NANO LETTERS

pubs.acs.org/NanoLett Letter

Manipulating Oxidation of Silicon with Fresh Surface Enabling Stable Battery Anode

Gaofeng Ge,[‖] Guocheng Li,[‖] Xiancheng Wang, Xiaoxue Chen, Lin Fu, Xiaoxiao Liu, Eryang Mao, Jing Liu, Xuelin Yang, Chenxi Qian, and Yongming Sun*

Cite This: *Nano Lett.* 2021, 21, 3127−3133 Read Online

ABSTRACT: Silicon (Si)-based material is a promising anode material for next-generation lithium-ion batteries (LIBs). Herein, we report the fabrication of a silicon oxide−carbon (SiO_x/C) nanocomposite through the reaction between silicon particles with fresh surface and H_2O in a mild hydrothermal condition, as well as conducting carbon coating synchronously. We found that controllable oxidation could be realized for Si particles to produce uniform SiO_x after the removal of the native passivation layer. The uniform oxidation and conductive coating offered the as-fabricated SiO_x/C composite good stability at both particle and electrode level over electrochemical cycling. The as-fabricated SiO_x/C composite delivered a high reversible capacity of 1133 mAh g^{-1} at 0.5 A g^{-1} with 89.1% capacity retention after 200 cycles. With 15 wt % SiO_x/C composite, graphite-SiO_x/C hybrid electrode displayed a high reversible specific capacity of 496 mAh g^{-1} and stable electrochemical cycling with a capacity retention of 90.1% for 100 cycles.

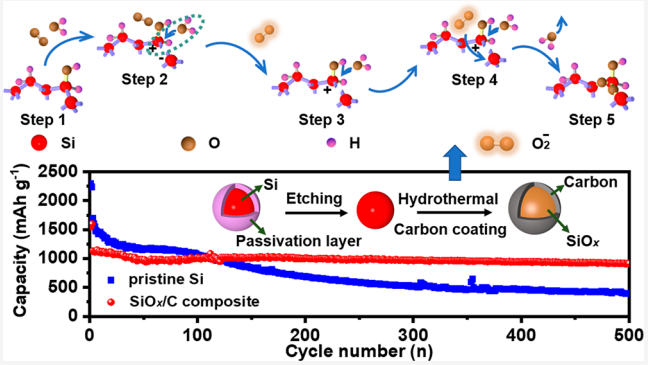

KEYWORDS: *lithium-ion batteries, silicon-based anode, controllable oxidation, capacity, cycling stability*

Lithium-ion batteries (LIBs) have been widely used as dominating power sources in portable electronics and are penetrating into the electrochemical vehicles and grid energy storage.[1−4] The ever-increasing energy demand requires higher energy density of LIBs, which requires the development of new electrode materials with higher capacity.[5−9] In the past years, research has been widely conducted on Si-based materials to replace the traditional graphite anode materials due to their much higher theoretical capacity (4200 mAh g^{-1} for Si versus 372 mAh g^{-1} for graphite), low cost, and abundance in resources.[10−13] Unfortunately, the commercial application of Si-based materials is hindered by several severe issues, including low electrical conductivity, dramatic volume change (>300%), and unstable solid electrolyte interphase (SEI).[14−16] Intrinsically, large volume expansion and contraction during the lithiation/delithiation processes cause the fracture and pulverization of Si at both the particle and electrode levels, and thus the inferior cycling stability.[7,17] Meanwhile, fresh surface of Si is exposed accompanied by the fracture of the originally formed SEI, where new SEI reforms in the following charge/discharge cycles. Such a process consumes active lithium and electrolyte continuously and the as-formed thick SEI weakens the lithium-ion diffusion, which further results in degradation of electrochemical performance.[18] Although Si nanoparticles (Si NPs) can effectively avoid the particle fracture,[7] the problem of serious side reactions still exists due to its high surface area, leading to continuous consumption of active Li and electrolyte, growth of thick SEI, and an increase of electrode impedance (Figure S1a).[18−20]

Effectively addressing the inherent problems of Si NPs, Si/C nanocomposites have triggered extensive scientific research.[21−25] They can not only improve the electrical conductivity but also alleviate the volume change upon cycling processes, exhibiting improved electrochemical performance.[26,27] On the other hand, silicon suboxides (SiO_x) show outstanding virtue of less volume expansion/shrinkage in comparison to Si and can suppress the undesirable side reactions and improve the electrochemical cycling stability.[28−30] The oxygen in SiO_x can react with Li^+ generating inactive Li_2O and lithium silicates during the initial lithiation process, which are beneficial for buffering volume expansion and maintaining structural stability of the active material during cycling.[28,30] Meanwhile, the SEI layer formed on the surface of the SiO_x anode is more stable and intact than that on pure Si (Figure S1b). Therefore, although the specific capacity

Received: January 26, 2021
Revised: March 15, 2021
Published: March 18, 2021

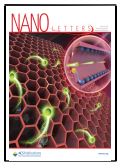

https://doi.org/10.1021/acs.nanolett.1c00317
Nano Lett. 2021, 21, 3127−3133

of SiO_x is somehow reduced in comparison to pure Si, the cycling stability is remarkably enhanced. With the combined advantage of composite of SiO_x and carbon, SiO_x/C nanocomposites have been shown their advantage in realizing stable electrode with reasonably high capacity, exhibiting good commercial application prospect (Figure S1c).[31,32] However, to date there lacks a facile and mild approach to regulate the oxygen content in SiO_x during the material's fabrication. A low content of oxygen cannot guarantee the effective suppression of volume change while a high content of oxygen would result in severe capacity reduction and large voltage hysteresis in voltage curves.[28]

Herein, we reveal the important role of fresh surface in regulating the oxidation of Si and realizing controllable oxidation and in situ carbon coating to form SiO_x/C composites though a facile one-step hydrothermal process and subsequent carbonization using Si waste from solar photovoltaic industry as the raw material. The prepared material featured a uniform composite of SiO_x and carbon. The uniform oxidation and in situ carbon coating are beneficial for improving the electrochemical performance of Si-based anodes for LIBs. As expected, the as-obtained SiO_x/C composite anode not only delivers high specific capacity but also manifests excellent cycling stability, thus providing a feasible approach for fabricating high-performance anodes for the forthcoming generation LIBs.

■ RESULTS AND DISCUSSION

There exists a dense layer of SiO_x on the bare Si surface (Figure 1a). This dense passivation layer insulates the active silicon from oxygen in the environment and inhibits further oxidation. Thus, bare Si particles cannot be oxidized under hydrothermal condition (Figure S2a, b). After the removal of the passivation layer, Si particles with a fresh surface is easily oxidized into SiO_x under a mild hydrothermal condition and the oxidation process and degree can be easily regulated. Besides, synchronous carbon coating was realized by introducing carbon sources into the solution for hydrothermal treatment and the SiO_x/C composite was fabricated after further annealing (Figure 1b).

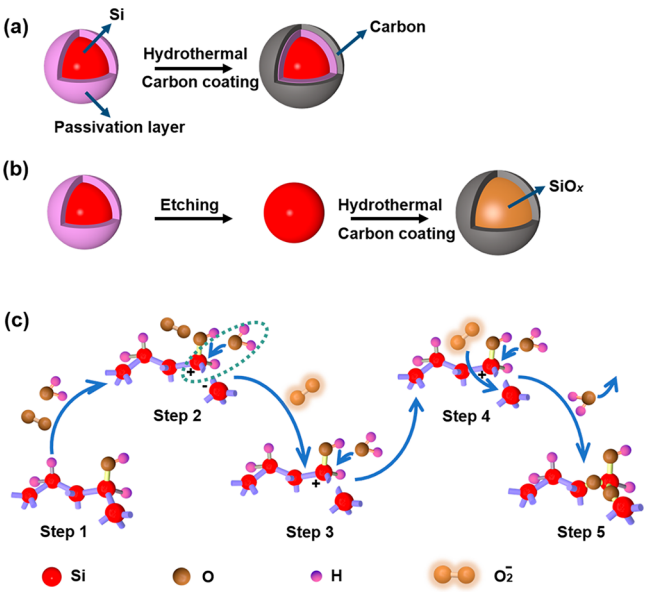

Figure 1. (a) Dense passivation layer on the Si surface, which prevents its further oxidation. (b) Schematic illustration of controllable oxidation of Si with fresh surface and synchronous carbon coating. (c) Schematic of the controllable oxidation under hydrothermal condition for Si particles with a fresh surface.

After the removal of the native passivation layer on the Si particle, one can easily regulate the oxidation of Si. On the basis of the framework of Cabrera−Mott mechanism, the controllable oxidation process under a hydrothermal condition is illustrated (Figure 1c).[33] Numerous highly reactive water and oxygen molecules surround the surface of uncontaminated Si. Polar water molecules preferentially adhere to the surface silanol groups, inducing the break of neighboring Si—Si bond adjacent to Si—OH bond due to its strong polarity while without any damage to the hydrophobic Si—H surface bonds (step 2). Then an electron from the broken chemical bond transfers to the adhesive O_2 and makes it electronegative (step 3). Driven by the generated electrostatic potential, the resultant O_2^- migrates toward the broken Si—Si bond (step 4), which causes the oxidation of this chemical bond and an adjacent Si—Si bond (step 5).[33] Here, the etching of pristine passivation layer of bare Si overturns the feasibility of the above-mentioned surface chemical evolution and favors for *in situ* fabrication of C coating layer. In addition, elevated pressure and high humidity provided by hydrothermal treatment further exacerbate the kinetics and thermodynamics of oxidation behavior.

Si waste from the photovoltaic industry was used as the Si resource for the fabrication of SiO_x/C composite. The Si powder before (namely initial Si) and after (namely pristine Si) the removal of the passivation layer showed similar morphology of irregular particles with size range between 100 to 300 nm observed from scanning electron microscopy (SEM, Figure S3a,b). The SiO_x/C composite was successfully fabricated after the hydrothermal treatment of Si particles with fresh surface and the following thermal annealing in Ar atmosphere. X-ray diffraction (XRD) pattern of the SiO_x/C composite demonstrate typical characteristic peaks at 28.4, 47.3, 56.1, 69.1, 76.4, and 88.0° for crystalline Si (PDF #99-0092) and a broad bump at ∼23° arising from the silicon oxide (Figure 2a).[21,34] In contrast, only crystalline Si phase was observed for the pristine Si. A broad XRD peak indicative for silicon oxidation was shown for Si particles with fresh surface after the same treatment as the SiO_x/C composite except for C coating (Figure S4a). This result indicates an ineligible amount of oxidation of Si with fresh surface during the hydrothermal treatment. With the increase of oxidation degree of silicon, the peak for silicon oxidation was obviously enhanced, accompanied by reduced intensity of the characteristic peaks for crystalline Si (Figure S4b). According to the electron probe microanalysis (EPMA), oxygen content in initial Si and SiO_x/C composite was 5.7 wt % and 22.7 wt %, respectively. Calculated based on the result of thermogravimetric analysis (TGA), the carbon content in the SiO_x/C composite was 15 wt % (Figure S5). X-ray photoelectron spectroscopy (XPS) was conducted to verify the chemical state evolution of Si from the pristine Si to the SiO_x/C composite. Signals for Si, O, and C elements are observed for the SiO_x/C composite (Figure S6a), suggesting the elemental components of the product. The strong carbon signal indicates the successful surface carbon coating on Si particles (Figure S6b). The Si signal is relatively weak since XPS detects the information on materials surface and SiO_x is protected by the surficial carbon layer/

https://doi.org/10.1021/acs.nanolett.1c00317
Nano Lett. 2021, 21, 3127−3133

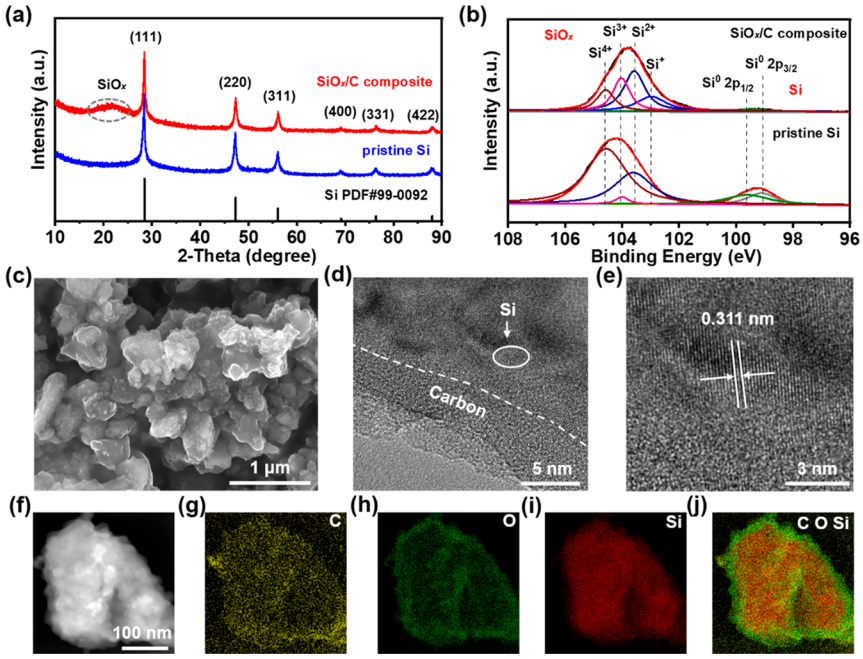

Figure 2. (a) XRD patterns of the starting Si material and the SiO_x/C composite. (b) High-resolution Si 2p XPS spectra of the pristine Si and the SiO_x/C composite. (c) SEM image of the SiO_x/C composite. (d) High-magnification TEM and (e) HRTEM image of the SiO_x/C composite (enlarged view of the circled area in panel d). (f) HAADF-STEM image of a SiO_x/C composite particle, and (g−j) the corresponding EDS elemental mapping images of Si, O, and C elements.

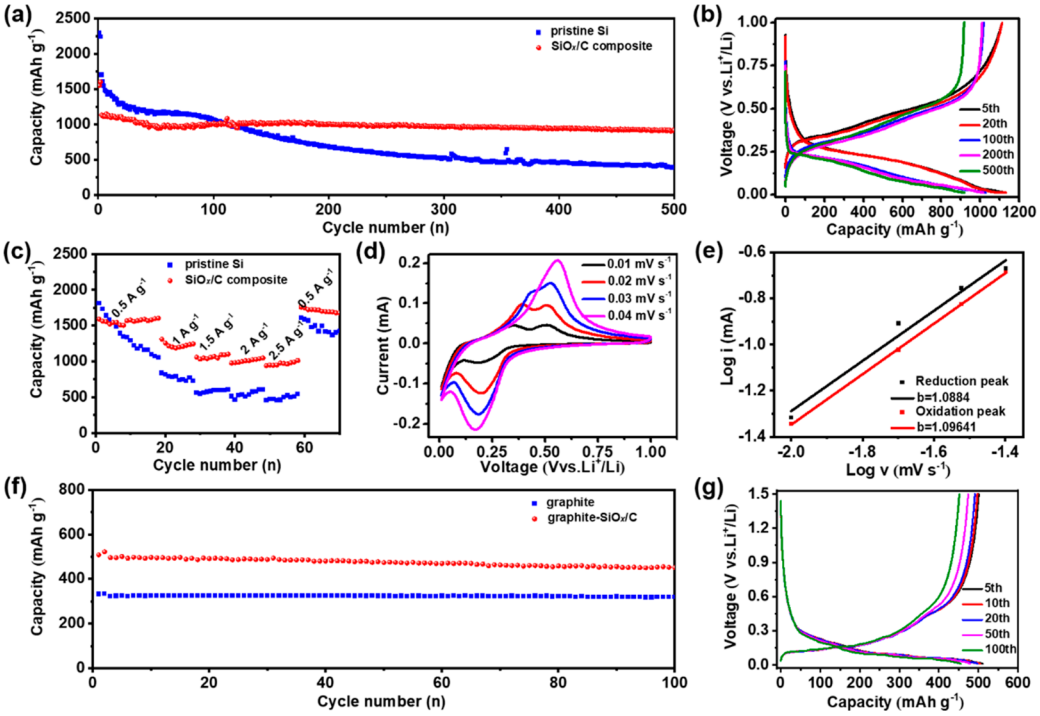

Figure 3. Electrochemical performance of the SiO_x/C composite. (a) Capacity-cycle number plots of the SiO_x/C composite and pristine Si at 0.5 A g^{-1}. The current density for the initial two activation cycles is 0.05 A g^{-1}. (b) Voltage profiles of the SiO_x/C electrode at different cycles. (c) Rate capabilities of the SiO_x/C and pristine Si electrodes at various current densities from 0.5 to 2.5 A g^{-1}. (d) CV curves of the SiO_x/C electrode at different scan rates from 0.01 to 0.04 mV s^{-1}. (e) Determination of *b*-value through the fitted linear model of log *i* and log *v* on redox peaks of the SiO_x/C electrode. (f) Cycling performance of the graphite−SiO_x/C hybrid and pure graphite electrodes with the same areal capacity fixed at 1 mAh cm^{-2}. The electrodes were cycled at 0.02 A g^{-1} for the initial two activation cycles and at 0.08 A g^{-1} for the subsequent cycles. (g) Galvanostatic voltage profiles of the graphite−SiO_x/C electrode at different cycles.

embedded in the carbon matrix. In contrast, the pristine Si powder shows a very weak signal for C and the O signal comes from the surficial oxidation of the pure Si sample. In the high-resolution Si 2p XPS spectrum for the SiO_x/C composite (Figure 2b), a broad peak in the binding energy range of 101−107 eV is fitted to Si^+, Si^{2+}, Si^{3+} and Si^{4+}, showing various

https://doi.org/10.1021/acs.nanolett.1c00317
Nano Lett. 2021, 21, 3127−3133

oxidation states of the amorphous SiO_x. The intensity for Si^0 peak in the range of 97−101 eV is negligible, suggesting the considerable oxidation of Si in the SiO_x/C composite. In contrast, the bare Si shows obvious peaks for both SiO_x and Si, suggesting the slight oxidation of Si during its rest in the ambient condition. The significantly enhanced intensity of peak related to SiO_x and weakened intensity of peak to Si−Si bond in the SiO_x/C sample indicate that crystalline Si suffers oxidation during the fabrication. The morphology and structure information on the SiO_x/C composite have been investigated by scanning electron microscope (SEM) and transmission electron microscope (TEM) coupled with energy dispersive X-ray (EDX) elemental mapping. The SiO_x/C composite image shows densely packed secondary particles with amorphous carbon coating (Figure S7) in the size of several micrometers (Figures 2c and S7), which is quite different from that of the pristine Si particles with loose agglomeration (Figure S3b). Transmission electron microscope (TEM) investigation was further conducted to investigate the structure and component of the SiO_x/C composite and pristine Si (Figures S9 and S10). The dark area and gray area corresponded to SiO_x nanoparticles and the carbon in the TEM image, respectively (Figure 2d and S9). The results show that the SiO_x nanoparticles were uniformly embedded in a carbon matrix in the composite secondary particle. In the high-resolution TEM image, the crystalline region with 3.1 Å spacing lattice fringe was observed, which ascribed to the (111) plane for Si. These crystalline regions were surrounded by amorphous regions (Figure 2e), again revealing the partial oxidation of Si in the SiO_x/C composite. To further investigate the microstructure of the SiO_x/C composite, the high-angle annular dark-field scanning transmission electron microscopy (HAADF-STEM) and element mapping were performed. As shown in Figure 2f−j, several SiO_x particles were embedded in a carbon matrix in a SiO_x/C composite particle. Si and O elements were evenly distributed throughout the core of the SiO_x/C composite particle, indicating uniform oxidation of Si. A line scanning test for Si, O, and C elements was further conducted (Figure S11). The results indicated that the signal of C went across the entire scan line, confirming the intact carbon coating layer on SiO_x particles, which provided good conductivity and worked the volume change buffer structure for the SiO_x/C nanocomposite.

The electrochemical performance of the as-fabricated SiO_x/C composite was investigated by galvanostatic charge/discharge measurement. All mentioned capacities are based on the mass of the SiO_x/C composite in the electrode. Figure 3a shows the capacity-cycle number plots for the SiO_x/C composite and pristine Si electrodes cycled at 0.5 A g^{-1}. Although the partial oxidation of Si to SiO_x and the introduction of carbon decrease the capacity to a certain extent, the cycling stability of the SiO_x/C composite is significantly enhanced in comparison to the pristine Si. A reversible specific capacity of 1133 mAh g^{-1} was achieved for the SiO_x/C electrode at 0.5 A g^{-1} after the initial two activation cycles at 0.05 A g^{-1}. After 500 cycles, the reversible capacity of the SiO_x/C composite was still at 917 mAh g^{-1}, with a capacity retention of 80.9% and a capacity decay rate of 0.038%. In contrast, although the pristine Si electrode displays a high initial capacity of 1699 mAh g^{-1}, it lost nearly all its capacity after 500 cycles, showing a very low capacity retention of 23.5%. Here, the Si was appropriately oxidized in the SiO_x/C composite, achieving a dynamic balance between capacity and cycling stability. Once the Si was overoxidized, the capacity dropped drastically (Figure S12). The uniform oxidation of Si is beneficial for buffering the volume change during the repeated alloy/dealloy reactions and improving the stability of active materials. Also, the carbon framework not only provides good electronic conductivity but also suppresses the side reactions between the active materials and electrolyte. Therefore, the electrochemical stability of the SiO_x/C composite is much enhanced. The galvanostatic voltage profiles of the SiO_x/C composite electrode demonstrated characteristic voltage plateaus of Si-based materials (Figures 3b and S13). The voltage profiles overlapped well for the initial 20 cycles for the SiO_x/C composite electrode. These characteristic voltage profiles remained for 500 cycles with only slightly increased voltage polarization due to the decay of the counter Li metal electrode in the SiO_x/C||Li half cell. This result illustrated prominent cycling stability of the SiO_x/C electrode. In contrast, large voltage polarization was observed for the pristine Si electrode after only five cycles (Figure S14). The superiority in electrochemical performance of the as-fabricated SiO_x/C composite to pristine Si was also verified by their distinct rate capability (Figure 3c). Except for the first four cycles, the SiO_x/C electrode delivered a higher specific capacity than the pristine Si electrode under almost all of the tested current density conditions. For example, the reversible specific capacity was 970 mAh g^{-1} for the SiO_x/C electrode at 2.5 A g^{-1}, which was significantly higher than 498 mAh g^{-1} for pristine Si electrode (Figure 3c). The voltage profiles of two samples at different current density were also compared, further verifying the advance of the SiO_x/C composite in rate capacity (Figure S15a,b). Higher overpotential and faster capacity decay for the pristine Si can be attributed to the sluggish kinetics of alloy/dealloy reactions. For the SiO_x/C composite, the carbon matrix enhanced the conductivity of the entire material and enabled fast reaction kinetics.

To further investigate the structural advantage of the SiO_x/C composite in reaction kinetics during the electrochemical measurement, cyclic voltammetry (CV) investigation was conducted for the SiO_x/C composite and the pristine Si electrodes in the voltage range of 0.01−1 V with different scan rates from 0.01 to 0.04 mV s^{-1}. The CV profiles were recorded and analyzed as shown in Figure 3d and Figure S16a. At all measured rates for the SiO_x/C composite, there existed a main cathodic peak at ∼0.2 V and two main anodic peaks at ∼0.4 and ∼0.5 V, respectively, corresponding to the alloying and dealloying processes of the Li_xSi phases (Figure 3d). For the pristine Si electrode, an additional peak at ∼0.1 V was recorded, which might be ascribed to the insertion of Li^+ into polycrystalline silicon (Figure S16a).[35,36] According to previous research, the correlation between scan rates (v) and peak current (i) can be expressed by a power-law function[37,38]

$$i = av^b$$

$$\log i = b \log v + \log a$$

where a and b represent variable parameters. Generally, the b-value of 0.5 indicates a diffusion-controlled interfacial reaction behavior while a b-value of 1 implies a nondiffusion controlled capacitive process.[39,40] On the basis of the fitted linear model of log i and log v in which the slopes represented b-values, the slopes of reduction and oxidation peaks were fitted to 1.0884 and 1.09641 for the SiO_x/C composite (Figure 3e), illustrating the kinetics dominated by a capacitive process. The analogous

https://doi.org/10.1021/acs.nanolett.1c00317
Nano Lett. 2021, 21, 3127−3133

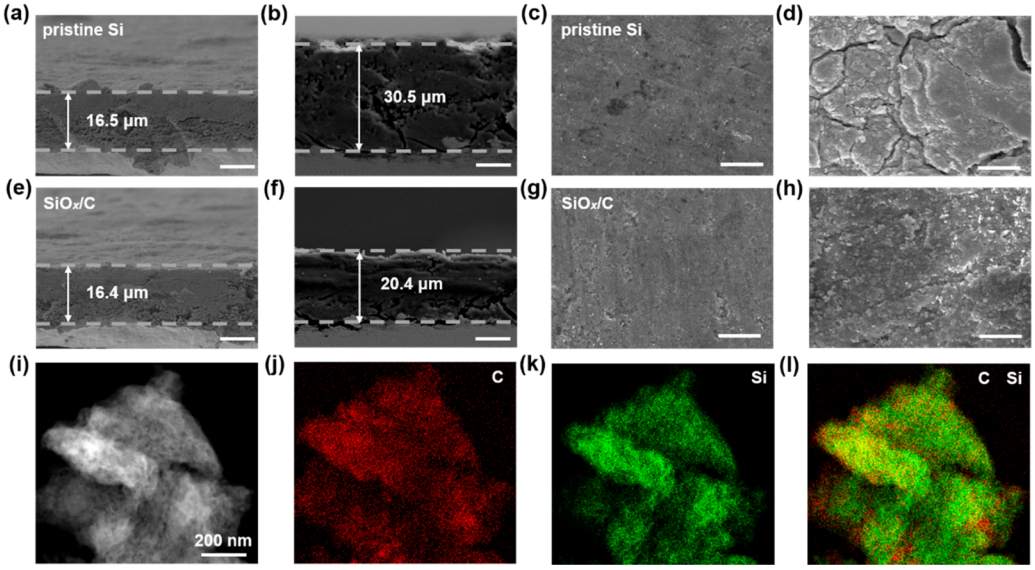

Figure 4. Cross-sectional and top-view SEM images of the pristine Si electrode (a,c) before and (b,d) after 50 cycles at 0.5 A g^{-1}. Cross-sectional and top-view SEM images of the SiO_x/C electrode (e,g) before and (f,h) after 50 cycles at 0.5 A g^{-1} (scale bar, 10 μm). (i) HAADF-STEM and (j−l) corresponding EDS elemental mapping images of the SiO_x/C electrode after 100 cycles at 0.5 A g^{-1}.

values for the pristine Si electrode were 0.61738 and 0.51119 (Figure S16b), respectively, indicating that the kinetics were primarily diffusion-controlled interfacial reaction behaviors. These results intrinsically validate the enhanced reaction kinetics of the SiO_x/C composite in comparison to the pristine Si.

Electrochemical impedance spectroscopy (EIS) was further conducted to verify the good electrochemical stability of the SiO_x/C composite. In the Nyquist plots shown in Figure S17, the irregular semicircle at high-medium frequency range represented the interface resistance of SEI and the charge transfer resistance at the electrode surface, and the oblique straight line at the low frequency range indicated the ion conductivity of the electrode. After the initial active cycles, the value of the interface resistance of the SiO_x/C composite was ∼100 Ω, which was significantly smaller than that of the pristine Si (Figure S17a). After 50 cycles, the interface resistance of the SiO_x/C composite remained stable, indicating its good interface stability and stable SEI structure. The oxidation of Si relieves the volume change during the lithiation/delithiation processes, and the *in situ* formed carbon matrix enhanced the conductivity and isolated the direct contact between Si and electrolyte, thus resulting in a stable SEI. In contrast, the pristine Si anode showed quick increase in interface resistance, indicating the overincreasing thickness of the SEI due to the continuous side reactions between the electrolyte and materials upon cycling (Figure S17b). Correspondingly, the charge transfer resistance of the SiO_x/C electrode was evidently lower than that of the pristine Si electrode due to the introduction of *in situ* formed carbon matrix, which could provide abundant charge transfer channels. To show the practical application of the SiO_x/C composite for the next-generation LIBs, graphite-SiO_x/C hybrid electrodes were fabricated. The battery cycling was performed at a current density of 0.02 A g^{-1} for the first two cycles and 0.08 A g^{-1} for the subsequent cycles in Li metal half-cell configuration (Figure 3f). Owing to the high specific capacity of SiO_x/C composite, the graphite-SiO_x/C hybrid with 15 wt % SiO_x/C composite showed significantly increased capacity than the pure graphite. The graphite-SiO_x/C hybrid delivered a high reversible specific capacity of 496 mAh g^{-1}, 50% higher than that of the tested graphite. Meanwhile, graphite-SiO_x/C hybrid displayed stable cycling with capacity retention of 90.1% after 100 cycles with fixed areal capacity loading of 1 mAh cm^{-2}. Observed from the voltage-capacity plots, voltage curves of the graphite-SiO_x/C hybrid for different cycles overlapped well, and the trend was in good agreement with that of pure graphite, suggesting good stability during cycling (Figures 3g and S18). The result above indicates the important role of the SiO_x/C composite in improving the state-of-art LIBs and sheds light on its potential application in the next-generation high-energy-density LIBs.

To verify the good stability of the SiO_x/C composite, the SiO_x/C composite and pristine Si electrodes with similar mass loading (0.9 mg cm^{-2}) after cycling were investigated. As shown by the cross-sectional SEM images, the thickness of the pristine Si electrode dramatically increased from 16.5 to 30.5 μm after 50 cycles (Figure 4a, b). Moreover, the top-view SEM images showed rough surface for the pristine Si electrode due to the coverage of a thick SEI, and severe cracks were observed (Figure 4c,d). These results indicated the rapid mechanical degradation of electrodes during cycling due to the repeated large volume expansion and shrinkage, and continuous side reactions during cycling. In sharp contrast, the SiO_x/C electrode displayed a slight increase in thickness from 16.4 to 20.4 μm after 50 cycles (Figure 4e,f) and its surface remained smooth without very thick SEI and large cracks (Figure 4g,h). This result indicated the excellent stability of the SiO_x/C composite electrode during cycling benefited from the advantage of low volume change ratio of SiO_x in comparison to pristine Si and buffering effect of the carbon matrix. The investigation on the morphology and structure of the SiO_x/C composite after cycling was further conducted by high-angle annular dark-field scanning transmission electron microscope (HADDF-STEM) and elemental mapping images. Even after 100 cycles at 0.5 A g^{-1}, the initial structure of SiO_x in the carbon matrix was well preserved without collapsion or rupture (Figure 4i−l). It was observed that the elemental signal for Si

https://doi.org/10.1021/acs.nanolett.1c00317
Nano Lett. 2021, 21, 3127−3133

signal and C overlapped well in a composite particle and the composite particle maintained its structure without facture, suggesting that the active SiO_x was well protected by the carbon matrix and the volume change was effectively suppressed during the long-term cycling. Because of the regulated oxidation of Si, lithium silicates irreversibly form during the initial lithiation process of SiO_x, which functions as a lithium-ion conductive flexible matrix. Moreover, the carbon matrix also can provide physical confinement for the active material, and alleviate the direction contact between electrolyte and active material, thus stabilizing the SEI layer and eventually improve the overall electrochemical performance of Si electrode.

■ CONCLUSION

We explored a facile approach to regulate the oxidation of Si particles in a mild condition. Experimentally, we fabricated a SiO_x/C composite with controlled oxidation degree using Si particles with fresh surface under a mild hydrothermal condition followed by thermal annealing. The as-fabricated SiO_x/C composite featured active SiO_x particles embedded in a carbon matrix, which enhanced the reaction kinetics and greatly relieved volume variation at both the particle and electrode level. As expected, the SiO_x/C composite maintained good structural integrity and electrochemical stability for over 100 charge/discharge cycles. When mixed with graphite, a graphite-SiO_x/C hybrid electrode with 15 wt % SiO_x/C displayed a much higher capacity of 496 mAh g^{-1} than the pure graphite and a high capacity retention of 90.1% for 100 cycles. Therefore, the SiO_x/C composite exhibits an indelible important promotion for the commercial application of high-capacity Si-based anode for the next generation of high-energy lithium-ion batteries.

■ ASSOCIATED CONTENT

Supporting Information

The Supporting Information is available free of charge at https://pubs.acs.org/doi/10.1021/acs.nanolett.1c00317.

Experimental details and additional characterizations (PDF)

■ AUTHOR INFORMATION

Corresponding Author

Yongming Sun − *Wuhan National Laboratory for Optoelectronics, Huazhong University of Science and Technology, Wuhan 430074, China;* orcid.org/0000-0001-8528-525X; Email: yongmingsun@hust.edu.cn

Authors

Gaofeng Ge − *Wuhan National Laboratory for Optoelectronics, Huazhong University of Science and Technology, Wuhan 430074, China*

Guocheng Li − *Wuhan National Laboratory for Optoelectronics, Huazhong University of Science and Technology, Wuhan 430074, China*

Xiancheng Wang − *Wuhan National Laboratory for Optoelectronics, Huazhong University of Science and Technology, Wuhan 430074, China*

Xiaoxue Chen − *Wuhan National Laboratory for Optoelectronics, Huazhong University of Science and Technology, Wuhan 430074, China*

Lin Fu − *Wuhan National Laboratory for Optoelectronics, Huazhong University of Science and Technology, Wuhan 430074, China;* orcid.org/0000-0001-6834-2881

Xiaoxiao Liu − *Wuhan National Laboratory for Optoelectronics, Huazhong University of Science and Technology, Wuhan 430074, China*

Eryang Mao − *Wuhan National Laboratory for Optoelectronics, Huazhong University of Science and Technology, Wuhan 430074, China*

Jing Liu − *Wuhan National Laboratory for Optoelectronics, Huazhong University of Science and Technology, Wuhan 430074, China*

Xuelin Yang − *College of Electrical Engineering and New Energy, China Three Gorges University, Yichang, Hubei 443002, China;* orcid.org/0000-0001-5626-701X

Chenxi Qian − *Division of Chemistry and Chemical Engineering, California Institute of Technology, Pasadena, California 91125, United States*

Complete contact information is available at: https://pubs.acs.org/10.1021/acs.nanolett.1c00317

Author Contributions

[‖]G.G. and G.L. contributed equally to this work.

Notes

The authors declare no competing financial interest.

■ ACKNOWLEDGMENTS

This work was supported by National Key R&D Program of China (2018YFB0905400), Major Technological Innovation Project of Hubei Science and Technology Department (2019AAA164). Y.S. acknowledges the financial support by the Innovation Fund of Wuhan National Laboratory for Optoelectronics of Huazhong University of Science and Technology. C.Q. acknowledges the support of the Natural Sciences and Engineering Research Council of Canada (NSERC Postdoctoral Fellowship). The authors would like to thank the Analytical and Testing Center of Huazhong University of Science and Technology (HUST) as well as the Center for Nanoscale Characterization and Devices of Wuhan National Laboratory for Optoelectronics (WNLO) for providing the facilities to conduct the characterizations.

■ REFERENCES

(1) Armand, M.; Tarascon, J. M. Building better batteries. *Nature* **2008**, *451*, 652−657.

(2) Schmuch, R.; Wagner, R.; Hörpel, G.; Placke, T.; Winter, M. Performance and cost of materials for lithium-based rechargeable automotive batteries. *Nat. Energy* **2018**, *3*, 267−278.

(3) Dunn, B.; Kamath, H.; Tarascon, J.-M. Electrical Energy Storage for the Grid: A Battery of Choices. *Science* **2011**, *334*, 928.

(4) Li, X.; Gu, M.; Hu, S.; Kennard, R.; Yan, P.; Chen, X.; Wang, C.; Sailor, M. J.; Zhang, J.-G.; Liu, J. Mesoporous silicon sponge as an anti-pulverization structure for high-performance lithium-ion battery anodes. *Nat. Commun.* **2014**, *5*, 4105.

(5) Choi, J. W.; Aurbach, D. Promise and reality of post-lithium-ion batteries with high energy densities. *Nat. Rev. Mater.* **2016**, *1*, 16013.

(6) Duan, J.; Zheng, Y.; Luo, W.; Wu, W.; Wang, T.; Xie, Y.; Li, S.; Li, J.; Huang, Y. Is graphite lithiophobic or lithiophilic. *Natl. Sci. Rev.* **2020**, *7*, 1208−1217.

(7) Sun, Y.; Liu, N.; Cui, Y. Promises and challenges of nanomaterials for lithium-based rechargeable batteries. *Nat. Energy* **2016**, *1*, 16071.

(8) Li, Y.; Wang, C.; Wang, W.; Eng, A. Y. S.; Wan, M.; Fu, L.; Mao, E.; Li, G.; Tang, J.; Seh, Z. W.; Sun, Y. Enhanced Chemical

Immobilization and Catalytic Conversion of Polysulfide Intermediates Using Metallic Mo Nanoclusters for High-Performance Li-S Batteries. *ACS Nano* **2020**, *14*, 1148−1157.

(9) Choi, S.-H.; Nam, G.; Chae, S.; Kim, D.; Kim, N.; Kim, W. S.; Ma, J.; Sung, J.; Han, S. M.; Ko, M.; Lee, H.-W.; Cho, J. Robust Pitch on Silicon Nanolayer-Embedded Graphite for Suppressing Undesirable Volume Expansion. *Adv. Energy Mater.* **2019**, *9*, 1803121.

(10) Zhu, B.; Liu, G.; Lv, G.; Mu, Y.; Zhao, Y.; Wang, Y.; Li, X.; Yao, P.; Deng, Y.; Cui, Y.; Zhu, J. Minimized lithium trapping by isovalent isomorphism for high initial coulombic efficiency of silicon anodes. *Sci. Adv.* **2019**, *5*, No. eaax0651.

(11) Xu, R.; Wang, G.; Zhou, T.; Zhang, Q.; Cong, H.-P.; Sen, X.; Rao, J.; Zhang, C.; Liu, Y.; Guo, Z.; Yu, S.-H. Rational design of Si@carbon with robust hierarchically porous custard-apple-like structure to boost lithium storage. *Nano Energy* **2017**, *39*, 253−261.

(12) An, W.; Gao, B.; Mei, S.; Xiang, B.; Fu, J.; Wang, L.; Zhang, Q.; Chu, P. K.; Huo, K. Scalable synthesis of ant-nest-like bulk porous silicon for high-performance lithium-ion battery anodes. *Nat. Commun.* **2019**, *10*, 1447.

(13) Yeom, S. J.; Lee, C.; Kang, S.; Wi, T. U.; Lee, C.; Chae, S.; Cho, J.; Shin, D. O.; Ryu, J.; Lee, H. W. Native Void Space for Maximum Volumetric Capacity in Silicon-Based Anodes. *Nano Lett.* **2019**, *19*, 8793−8800.

(14) Liu, T.; Chu, Q.; Yan, C.; Zhang, S.; Lin, Z.; Lu, J. Interweaving 3D Network Binder for High-Areal-Capacity Si Anode through Combined Hard and Soft Polymers. *Adv. Energy Mater.* **2019**, *9*, 1802645.

(15) Choi, S.; Kwon, T.-w.; Coskun, A.; Choi, J. W. Highly elastic binders integrating polyrotaxanes for silicon microparticle anodes in lithium ion batteries. *Science* **2017**, *357*, 279.

(16) Liu, N.; Lu, Z.; Zhao, J.; McDowell, M. T.; Lee, H.-W.; Zhao, W.; Cui, Y. A pomegranate-inspired nanoscale design for large-volume-change lithium battery anodes. *Nat. Nanotechnol.* **2014**, *9*, 187−192.

(17) Son, I. H.; Hwan Park, J.; Kwon, S.; Park, S.; Rümmeli, M. H.; Bachmatiuk, A.; Song, H. J.; Ku, J.; Choi, J. W.; Choi, J.-m.; Doo, S.-G.; Chang, H. Silicon carbide-free graphene growth on silicon for lithium-ion battery with high volumetric energy density. *Nat. Commun.* **2015**, *6*, 7393.

(18) Lin, D.; Lu, Z.; Hsu, P.-C.; Lee, H. R.; Liu, N.; Zhao, J.; Wang, H.; Liu, C.; Cui, Y. A high tap density secondary silicon particle anode fabricated by scalable mechanical pressing for lithium-ion batteries. *Energy Environ. Sci.* **2015**, *8*, 2371−2376.

(19) Jin, Y.; Zhu, B.; Lu, Z.; Liu, N.; Zhu, J. Challenges and Recent Progress in the Development of Si Anodes for Lithium-Ion Battery. *Adv. Energy Mater.* **2017**, *7*, 1700715.

(20) Lee, S. W.; Lee, H.-W.; Ryu, I.; Nix, W. D.; Gao, H.; Cui, Y. Kinetics and fracture resistance of lithiated silicon nanostructure pairs controlled by their mechanical interaction. *Nat. Commun.* **2015**, *6*, 7533.

(21) Zheng, G.; Xiang, Y.; Xu, L.; Luo, H.; Wang, B.; Liu, Y.; Han, X.; Zhao, W.; Chen, S.; Chen, H.; Zhang, Q.; Zhu, T.; Yang, Y. Controlling Surface Oxides in Si/C Nanocomposite Anodes for High-Performance Li-Ion Batteries. *Adv. Energy Mater.* **2018**, *8*, 1801718.

(22) Li, Y.; Yan, K.; Lee, H.-W.; Lu, Z.; Liu, N.; Cui, Y. Growth of conformal graphene cages on micrometre-sized silicon particles as stable battery anodes. *Nat. Energy* **2016**, *1*, 15029.

(23) Xu, Q.; Li, J.-Y.; Sun, J.-K.; Yin, Y.-X.; Wan, L.-J.; Guo, Y.-G. Watermelon-Inspired Si/C Microspheres with Hierarchical Buffer Structures for Densely Compacted Lithium-Ion Battery Anodes. *Adv. Energy Mater.* **2017**, *7*, 1601481.

(24) Wang, J.; Liao, L.; Li, Y.; Zhao, J.; Shi, F.; Yan, K.; Pei, A.; Chen, G.; Li, G.; Lu, Z.; Cui, Y. Shell-Protective Secondary Silicon Nanostructures as Pressure-Resistant High-Volumetric-Capacity Anodes for Lithium-Ion Batteries. *Nano Lett.* **2018**, *18*, 7060−7065.

(25) Ko, M.; Chae, S.; Ma, J.; Kim, N.; Lee, H.-W.; Cui, Y.; Cho, J. Scalable synthesis of silicon-nanolayer-embedded graphite for high-energy lithium-ion batteries. *Nat. Energy* **2016**, *1*, 16113.

(26) Chae, S.; Choi, S.-H.; Kim, N.; Sung, J.; Cho, J. Integration of Graphite and Silicon Anodes for the Commercialization of High-Energy Lithium-Ion Batteries. *Angew. Chem., Int. Ed.* **2020**, *59*, 110−135.

(27) Li, X.; Yan, P.; Xiao, X.; Woo, J. H.; Wang, C.; Liu, J.; Zhang, J.-G. Design of porous Si/C-graphite electrodes with long cycle stability and controlled swelling. *Energy Environ. Sci.* **2017**, *10*, 1427−1434.

(28) Liu, Z.; Yu, Q.; Zhao, Y.; He, R.; Xu, M.; Feng, S.; Li, S.; Zhou, L.; Mai, L. Silicon oxides: a promising family of anode materials for lithium-ion batteries. *Chem. Soc. Rev.* **2019**, *48*, 285−309.

(29) Fu, R.; Zhang, K.; Zaccaria, R. P.; Huang, H.; Xia, Y.; Liu, Z. Two-dimensional silicon suboxides nanostructures with Si nano-domains confined in amorphous SiO_2 derived from Siloxene as high performance anode for Li-ion batteries. *Nano Energy* **2017**, *39*, 546−553.

(30) Majeed, M. K.; Ma, G.; Cao, Y.; Mao, H.; Ma, X.; Ma, W. Metal-Organic Frameworks-Derived Mesoporous Si/SiO_x@NC Nanospheres as a Long-Lifespan Anode Material for Lithium-Ion Batteries. *Chem. - Eur. J.* **2019**, *25*, 11991−11997.

(31) Liu, Z.; Guan, D.; Yu, Q.; Xu, L.; Zhuang, Z.; Zhu, T.; Zhao, D.; Zhou, L.; Mai, L. Monodisperse and homogeneous SiO_x/C microspheres: A promising high-capacity and durable anode material for lithium-ion batteries. *Energy Storage Mater.* **2018**, *13*, 112−118.

(32) Xu, Q.; Sun, J.-K.; Yin, Y.-X.; Guo, Y.-G. Facile Synthesis of Blocky SiO_x/C with Graphite-Like Structure for High-Performance Lithium-Ion Battery Anodes. *Adv. Funct. Mater.* **2018**, *28*, 1705235.

(33) Pereira, R. N.; Rowe, D. J.; Anthony, R. J.; Kortshagen, U. Oxidation of freestanding silicon nanocrystals probed with electron spin resonance of interfacial dangling bonds. *Phys. Rev. B: Condens. Matter Mater. Phys.* **2011**, *83*, 155327.

(34) Lee, S. J.; Kim, H. J.; Hwang, T. H.; Choi, S.; Park, S. H.; Deniz, E.; Jung, D. S.; Choi, J. W. Delicate Structural Control of Si-SiO_x-C Composite via High-Speed Spray Pyrolysis for Li-Ion Battery Anodes. *Nano Lett.* **2017**, *17*, 1870−1876.

(35) Magasinski, A.; Dixon, P.; Hertzberg, B.; Kvit, A.; Ayala, J.; Yushin, G. High-performance lithium-ion anodes using a hierarchical bottom-up approach. *Nat. Mater.* **2010**, *9*, 353−358.

(36) Li, P.; Hwang, J.-Y.; Sun, Y.-K. Nano/Microstructured Silicon-Graphite Composite Anode for High-Energy-Density Li Ion Battery. *ACS Nano* **2019**, *13*, 2624−2633.

(37) Augustyn, V.; Come, J.; Lowe, M. A.; Kim, J. W.; Taberna, P.-L.; Tolbert, S. H.; Abruña, H. D.; Simon, P.; Dunn, B. High-rate electrochemical energy storage through Li^C intercalation pseudocapacitance. *Nat. Mater.* **2013**, *12*, 518−522.

(38) Wang, L.; Jiang, B.; Vullum, P. E.; Svensson, A. M.; Erbe, A.; Selbach, S. M.; Xu, H.; Vullum-Bruer, F. High Interfacial Charge Storage Capability of Carbonaceous Cathodes for Mg Batteries. *ACS Nano* **2018**, *12*, 2998−3009.

(39) Chao, D.; Zhu, C.; Yang, P.; Xia, X.; Liu, J.; Wang, J.; Fan, X.; Savilov, S. V.; Lin, J.; Fan, H. J.; Shen, Z. X. Array of nanosheets render ultrafast and high-capacity Na-ion storage by tunable pseudocapacitance. *Nat. Commun.* **2016**, *7*, 12122.

(40) Sathiya, M.; Prakash, A. S.; Ramesha, K.; Tarascon, J. M.; Shukla, A. K. V_2O_5-Anchored Carbon Nanotubes for Enhanced Electrochemical Energy Storage. *J. Am. Chem. Soc.* **2011**, *133*, 16291−16299.

https://doi.org/10.1021/acs.nanolett.1c00317
Nano Lett. 2021, 21, 3127−3133